



HAL
open science

Correcting peak deformation in Rosetta's ROSINA/DFMS mass spectrometer

Johan de Keyser, Federik Dhooghe, Andrew Gibbons, Kathrin Altwegg, Hans Balsiger, Jean-Jacques Berthelier, Christelle Briois, Ursina Calmonte, Gael Cessateur, Eddy Equeter, et al.

► **To cite this version:**

Johan de Keyser, Federik Dhooghe, Andrew Gibbons, Kathrin Altwegg, Hans Balsiger, et al.. Correcting peak deformation in Rosetta's ROSINA/DFMS mass spectrometer. *International Journal of Mass Spectrometry*, 2015, 393, pp.41-51. 10.1016/j.ijms.2015.10.010 . insu-01219657

HAL Id: insu-01219657

<https://insu.hal.science/insu-01219657>

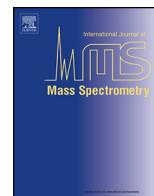
Submitted on 15 May 2020

HAL is a multi-disciplinary open access archive for the deposit and dissemination of scientific research documents, whether they are published or not. The documents may come from teaching and research institutions in France or abroad, or from public or private research centers.

L'archive ouverte pluridisciplinaire **HAL**, est destinée au dépôt et à la diffusion de documents scientifiques de niveau recherche, publiés ou non, émanant des établissements d'enseignement et de recherche français ou étrangers, des laboratoires publics ou privés.



Distributed under a Creative Commons Attribution - NonCommercial 4.0 International License



Correcting peak deformation in Rosetta's ROSINA/DFMS mass spectrometer



J. De Keyser^{a,b,*}, F. Dhooghe^a, A. Gibbons^{a,c}, K. Altwegg^{d,e}, H. Balsiger^d, J.-J. Berthelier^f, Ch. Briois^g, U. Calmonte^d, G. Cessateur^a, E. Equeter^h, B. Fietheⁱ, S.A. Fuselier^j, T.I. Gombosi^k, H. Gunell^a, M. Hässig^d, L. Le Roy^e, R. Maggiolo^a, E. Neefs^h, M. Rubin^d, Th. Sémon^d

^a Space Physics Division, Belgian Institute for Space Aeronomy, Ringlaan 3, B-1180 Brussels, Belgium

^b Center for Plasma Astrophysics, Katholieke Universiteit Leuven, Celestijnenlaan 200B, B-3001 Heverlee, Belgium

^c Quantum Chemistry and Photophysics Laboratory, Université Libre de Bruxelles, Av. F. D. Roosevelt 50, B-1050 Brussels, Belgium

^d Physikalisches Institut, University of Bern, Sidlerstr. 5, CH-3012 Bern, Switzerland

^e Center for Space and Habitability, University of Bern, Sidlerstr. 5, CH-3012 Bern, Switzerland

^f LATMOS/IPSL-CNRS-UPMC-UVSQ, 4 Av. de Neptune F-94100, Saint-Maur, France

^g Laboratoire de Physique et Chimie de l'Environnement et de l'Espace, CNRS & Univ. d'Orléans, 3A Av. de la Recherche Scientifique, 45071 Orléans, France

^h Engineering Division, Belgian Institute for Space Aeronomy, Ringlaan 3, B-1180 Brussels, Belgium

ⁱ Institute of Computer and Network Engineering (IDA), TU Braunschweig, Hans-Sommer-Straße 66, D-38106 Braunschweig, Germany

^j Department of Space Science, Southwest Research Institute, 6220 Culebra Road, San Antonio, TX 78228, USA

^k Department of Atmospheric, Oceanic and Space Sciences, University of Michigan, 2455 Hayward, Ann Arbor, MI 48109, USA

ARTICLE INFO

Article history:

Received 4 August 2015

Received in revised form 14 October 2015

Accepted 14 October 2015

Available online 23 October 2015

PACS:

82.80.Ms

95.55.Pe

95.55.Ym

95.75.Pq

MSC:

49M15

90C53

90C90

65K10

Keywords:

Mass spectrometry

Planetary instrumentation

Data analysis

Comet atmosphere

Rosetta

ABSTRACT

The Double Focusing Mass Spectrometer (DFMS), part of the ROSINA instrument package aboard the European Space Agency's Rosetta spacecraft visiting comet 67P/Churyumov-Gerasimenko, experiences minor deformation of the mass peaks in the high resolution spectra acquired for $m/Z = 16, 17$, and to a lesser extent 18. A numerical deconvolution technique has been developed with a twofold purpose. A first goal is to verify whether the most likely cause of the issue, a lack of stability of one of the electric potentials in the electrostatic analyser, can indeed be held responsible for it. The second goal is to correct for the deformation, in view of the important species located around these masses, and to allow a standard further treatment of the spectra in the automated DFMS data processing chain.

© 2015 The Authors. Published by Elsevier B.V. This is an open access article under the CC BY-NC-ND license (<http://creativecommons.org/licenses/by-nc-nd/4.0/>).

1. Introduction

DFMS is the high resolution double focusing mass spectrometer of the ROSINA instrument [1] onboard the Rosetta spacecraft of the European Space Agency. Rosetta is visiting comet 67P/Churyumov-Gerasimenko. The DFMS mass spectrometer (Fig. 1) has been built with the purpose of measuring the composition of the cometary

* Corresponding author at: Space Physics Division, Belgian Institute for Space Aeronomy, Ringlaan 3, B-1180 Brussels, Belgium. Tel.: +32 2 3730368.

E-mail address: Johan.DeKeyser@aeronomie.be (J. De Keyser).

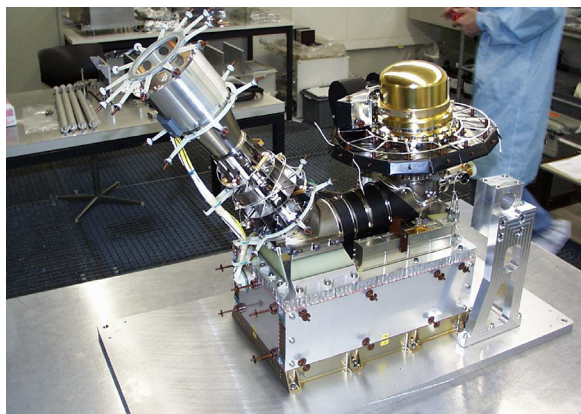


Fig. 1. The DFMS mass spectrometer in the clean room before installation on Rosetta. The instrument entrance is under the closed cover on the right; the detector head is to the left. The electronics box is at the bottom.

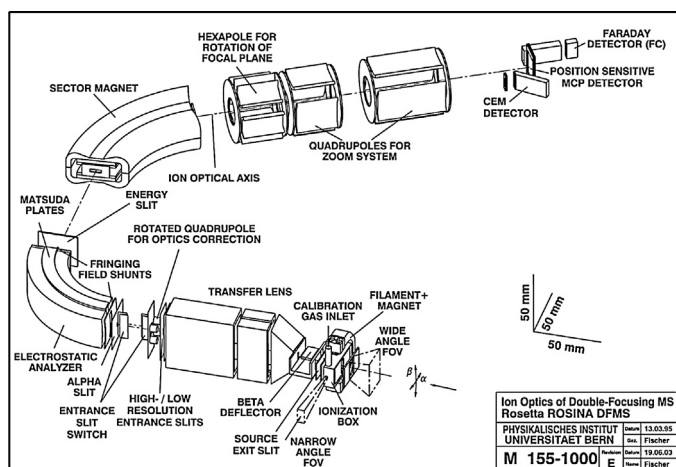


Fig. 2. A schematic drawing of the architecture of the DFMS mass spectrometer showing the instrument entrance with the ion source, the transfer optics, the electrostatic analyser, the sector magnet, the zoom system, and the detectors [1].

atmosphere. It can detect cometary neutrals and ions in the mass range of 13–150 amu/e. In the former case the neutrals flow into the instrument, where they may be ionised with or without accompanying fragmentation upon bombardment with 45 eV electrons. In the latter case, positive cometary ions are attracted by setting a grid in front of the instrument entrance at a negative potential, while the negative spacecraft potential also facilitates the ingestion of ions. The ions are electrostatically accelerated upon leaving the source. The analyser section (Fig. 2) consists of the transfer optics, an electrostatic analyser and a sector magnet, followed by a zoom system, allowing the instrument to work in a low and a high mass resolution mode (LR and HR mode), the HR mode offering a factor of 6.4 improvement in resolution as compared to the LR mode. The zoom system consists of a hexapole plus two quadrupoles. The hexapole can be used to rotate the focal plane, while the combination of two quadrupoles allows to increase the image scale. The actual zoom factor varies between 5.0 and 6.6 because the quadrupole potentials are adapted as a function of the accelerating potential [2]. DFMS features three different detectors, of which the combination of a microchannel plate (MCP) with a linear CCD (the Linear Electron Detector Array or LEDA chip, which for redundancy reasons features two rows of charge collecting anodes) is being used most often [3,4]. The analog CCD output is digitized by an analog-to-digital converter (ADC) providing a number of counts per pixel, which later is translated into a number of detected ions.

The DFMS-MCP/LEDA combination offers detailed views of sections of the mass range centered around a commanded mass. The mass resolution actually achieved is around $m/\Delta m = 800$ in LR mode and 5000 in HR mode, where Δm is the full width at half maximum of the mass peaks. The high resolution mode, in particular, offers interesting prospects for distinguishing isotopes and establishing isotope ratios [5,6]. Early scientific results [7–10] confirm the high mass resolution capability of the instrument.

While DFMS operates successfully, a problem has been spotted with the instrument operating in neutral mode for HR spectra at mass-over-charge ratios of $m/Z = 16, 17$, and to a lesser extent 18 amu/e; this problem is also marginally present in the LR spectra at $m/Z = 16$ and 17. The problem consists of an abnormal broadening and/or deformation of the mass peaks. Fig. 3 shows HR spectra for commanded masses $m/Z = 16$ amu/e (upper half of the figure) and $m/Z = 17$ amu/e (lower half) from row A (top) and B (bottom) obtained on 2014-08-22 02:10:40 and 02:11:08 (red \diamond), 2014-10-20 17:44:13 and 17:44:47 (green \circ), and 2014-12-25 11:17:34 and 11:18:04 (blue \square). All spectra were acquired with a high electron emission current (200 μ A) in the DFMS ion source. The curves give the raw ADC counts collected during 20 s after removal of the LEDA offset (pixel and read-out noise) as a function of the detector pixel number. The shape of the deformed peaks slowly changes with time. Within a single spectrum the peak shape is slightly different for each mass peak, and there also are some differences between row A and B. Peak positions also change with the properties of the mass analyser, for instance, due to the variation of magnet strength with temperature.

The most likely explanation offered thus far is a problem with the instrument optics. The electric potentials at which the inner and outer plates of the electrostatic analyser are set (as a function of commanded mass) are built from a coarse and a fine potential. Between $m/Z = 15$ and 16 amu/e there is a major step in the coarse potential, requiring the fine potential to be at its highest value for $m/Z = 16$ amu/e and progressively smaller at subsequent masses, and thus close to its design limits. The working hypothesis is that the fine potential then fluctuates around the desired value. The spectra therefore are deformed, and this is most pronounced in the HR spectra.

The goal of the present paper is (1) to model the peak deformation so as to verify whether it is compliant with the working hypothesis, and (2) to offer a way to deconvolve the spectra so that they can be processed afterwards by the normal DFMS data processing chain. This is particularly relevant in view of the importance of the species detected at $m/Z = 16$ –17 amu/e for cometary chemistry.

2. The origin of the peak deformation effect

This section first briefly reviews how DFMS mass spectra of neutral species are obtained with the MCP/LEDA detector. After that, the nature of the deformation is discussed.

2.1. DFMS mass spectra for neutral gas

DFMS is mounted on the comet-facing side of Rosetta with its $20^\circ \times 20^\circ$ field of view accepting the outflowing cometary gas. Neutral molecules can directly flow into the ion source where they are bombarded with electrons that are emitted by a filament and accelerated through a 45 V potential. A fraction of the molecules is ionised or broken up into charged fragments. These are accelerated by a mass-dependent acceleration voltage V_{accel} . The analyser has a Nier–Johnson geometry [11] in which a deflection of 90° in an electrostatic energy analyser is combined with a magnetic deflection of 60° . The analyser focuses ions with different entry angles but with the same energy, while ions with different energies are

spatially separated, after which the energy slit selects the desired energy range. The kinetic energy of the ions entering the analyser is (ignoring the initial ion energy in the ion source) the energy gained during acceleration

$$\frac{1}{2}mv^2 = ZeV_{\text{accel}}.$$

The ions follow a circular trajectory with radius r if they experience a constant radial acceleration

$$a = \frac{v^2}{r} = \frac{2ZeV_{\text{accel}}}{mr}$$

towards the circle center. Such a constant acceleration is provided in the circular electrostatic analyser section by the electric field set by the difference between the inner and outer electrostatic analyser plate potentials V_{outer} and V_{inner} ,

$$E_{\text{ESA}} = \frac{V_{\text{outer}} - V_{\text{inner}}}{\Delta R},$$

where ΔR is the width of the analyser channel. With $a = ZeE_{\text{ESA}}/m$, the radius of curvature of the ion trajectory is

$$r = \frac{2V_{\text{accel}}\Delta R}{V_{\text{outer}} - V_{\text{inner}}}.$$

The nominal design of the electrostatic analyser is such that $r = r_{\text{ESA}}$, that is, the curvature radius of the ions matches the curvature of the

circular analyser. If all is nominal, only ions within a given energy range around ZeV_{accel} arrive at the end of the circular section without hitting the walls, regardless of their mass. Note also that the energy of those ions does not change. An energy slit at the exit of the analyser narrows down the energy range even more (nominal energy $\pm 1\%$). At the same time, the exit velocities of the particles have become more precisely aligned. The magnetic sector with a field B and a radius r_{magnet} then sorts the ions according to m/Z . Ideally, ions with the commanded mass m/Z will hit the center of the detector as dictated by

$$\frac{m}{Ze} = \frac{r_{\text{magnet}}^2 B^2}{2V_{\text{accel}}}.$$

The DFMS optics allow for a high mass resolution mode by selecting a different slit after the transfer optics and by using a quadrupole-based zoom system. Also, to increase the sensitivity for heavy ions ($m/Z \geq 70$ amu/e) for which V_{accel} is low according to the above formula, a post-acceleration is applied by placing the front side of the MCP at a lower potential so that the ions gain additional energy before hitting the MCP. The MCP consists of two microchannel plates with narrow channels in a chevron shape. An incoming ion produces a cascade of electrons, the intensity of which depends on the ion energy and on the potential difference between the MCP front and back sides [3]. The resulting electron cascade then hits the 2-row 512-pixel LEDA chip [4]. The LEDA analog measurements are

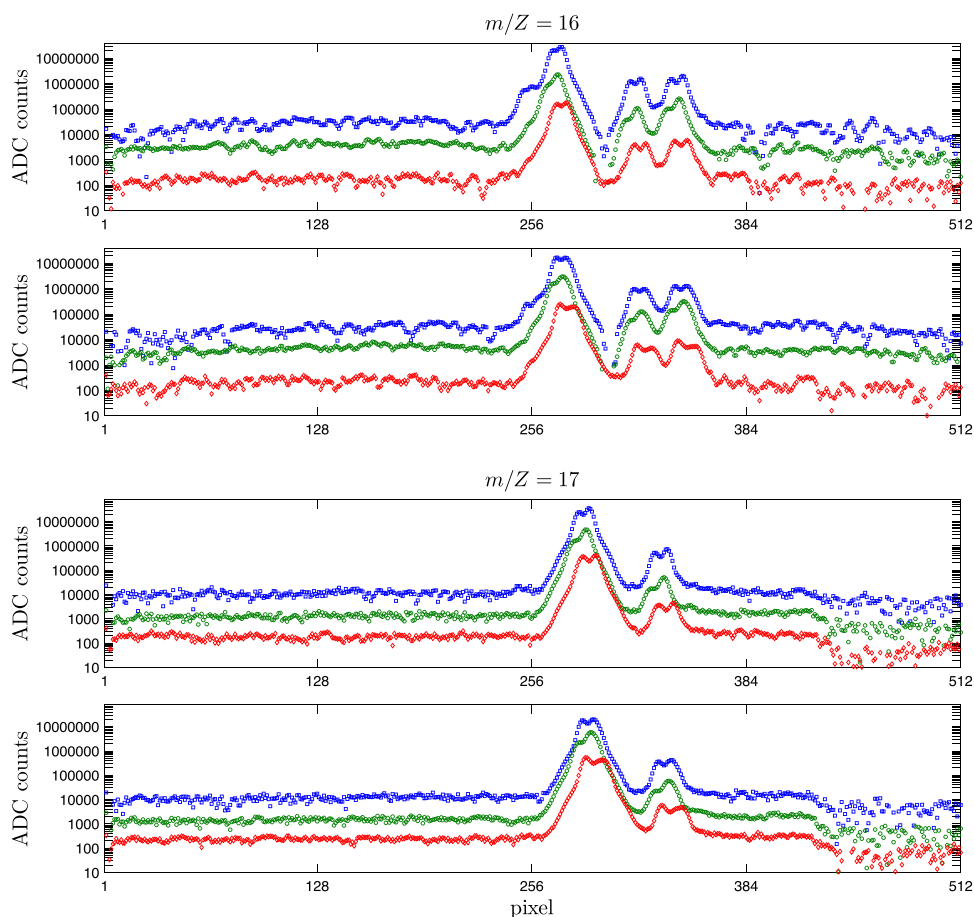


Fig. 3. High resolution DFMS-MCP/LEDA mass spectra for commanded masses $m/Z = 16$ amu/e (upper half of the figure) and $m/Z = 17$ amu/e (lower half) from row A (top) and B (bottom), obtained on 2014-08-22 02:10:40 and 02:11:08 (red \diamond), 2014-10-20 17:44:13 and 17:44:47 (green \circ), and 2014-12-25 11:17:34 and 11:18:04 (blue \square), showing double and/or deformed mass peaks. All spectra were acquired with a high electron emission current (200 μA) from the ion source filament. The curves give the raw ADC counts collected during 20 s (after removal of the offset due to pixel and read-out noise in the LEDA) as a function of detector pixel. For better visibility, the green line has been multiplied by 10 and the blue one by 100. The peak positions shift as a consequence not only of changing peak shape, but also due to changes in the mass analyser transmission properties, e.g. because of variations in magnet temperature. The pixel spacing is about 0.00052 amu/e, with the double peaks typically being 7 pixels apart. (For interpretation of the references to color in this figure legend, the reader is referred to the web version of this article.)

converted to a digital signal, and are obtained as ADC counts as a function of LEDA pixel number for both LEDA rows. The MCP/LEDA detector thus records a mass spectrum for an m/Z interval around the CM. All particles with the same m/Z produce a mass peak with a finite width due to the remaining spread in energy and/or velocity of the ions as they exit the analyser section, due to the size of the MCP microchannels, and also due to the finite width of the electron cascade recorded by the LEDA for each ion incident on the MCP, which depends on the MCP and LEDA pixel sizes and the MCP-LEDA separation. It turns out that mass peaks can be represented by a Gaussian at the nominal ion m/Z and a half-width of about 6 LEDA pixels, combined with a second Gaussian centered at the same m/Z , with $\sim 1/6$ th of the amplitude and a width that is ~ 2.5 times wider. Typically, a number of separate short-duration exposures is accumulated at the same CM, in order to produce a spectrum while averaging out noise. The ADC counts need to be corrected for the offset due to pixel and read-out noise in the LEDA, for the overall MCP gain factor, and for the pixel-dependent gain differences mainly due to uneven MCP aging. By taking into account the instrument sensitivities and the fragmentation patterns in the ion source, one may derive neutral comet gas densities [see, e.g., the discussion in 12]. For verification, at least for the major species (H_2O , CO , CO_2), a cross-calibration can be performed with the density measured by the COPS nude gauge and/or with the RTOF mass spectrometer [1].

2.2. Peak deformation

Assume that there is an error δE_{ESA} in the electric field applied in the analyser due to an ill-set voltage. If this error is small, an ion in a first approximation still follows a circular trajectory, but with a slightly modified radius

$$r' = r + \delta r = r \left(1 - \frac{\delta E_{\text{ESA}}}{E_{\text{ESA}}} \right).$$

This change in radial position of the ions upon leaving the analyser propagates further down the magnetic sector and the zoom system. Thus, the consequence of a slight change in the analyser potentials is a proportionally slight displacement of the mass spectra in LR mode, and a more pronounced displacement in HR mode as the effect is magnified by the zoom optics. This displacement results in an apparent change of mass.

Let us examine what happens if the analyser electric field, instead of being steady, fluctuates over a limited range. As an example, consider the fluctuation in the position of the mass peaks to be of the form

$$\delta m = \Delta m (\sin t - \beta \cos 2t) \quad (1)$$

where Δm is a parameter characterising the fluctuation amplitude, and where β is a dimensionless parameter. The apparent mass shifts between $\Delta m(-1 + \beta)$ and $\Delta m(1 + \beta)$ while the average value remains zero. As time progresses, the LEDA detector accumulates charges corresponding to the typical double-Gaussian mass peaks, while the shift changes continuously. This leads to “blurred” or “deformed” mass peaks.

For $\beta = 0$ the fluctuation is sinusoidal with amplitude Δm . Fig. 4, left column, shows the waveform, the distribution of δm , and the resulting mass peak shape for two different ratios of the double-Gaussian peak widths (w_1 is the width of the primary Gaussian, while the width of the secondary one is taken $w_2 = 2.5w_1$) relative to the fluctuation amplitude, $w_1/\Delta m = 1.28$ and 0.2 ; these ratios correspond to typical LR and HR mode spectra, respectively. For a sinusoidal fluctuation, the $\delta m/\Delta m$ distribution can be approximated by a binary distribution at ± 1 . Depending on the ratio $w_1/\Delta m$, this results in a broadened peak or a double

peak. For the case $\beta = 0.2$, shown in Fig. 4, middle column, the mass peaks are now peaks with a shoulder or asymmetric double peaks, and again the distribution is dominated by the two extreme amplitudes. A more complicated case is shown in Fig. 4, right column, for $\beta = 0.6$. The $\delta m/\Delta m$ distribution is now dominated by three values, and the mass peaks are deformed even more.

While the time variations of the imposed V_{inner} and V_{outer} are not known, they must change more rapidly than the time needed to collect a spectrum, and within a limited range. Whatever the precise waveform, one can conclude that the deformed peak shapes observed in the LR and HR spectra (double peaks, shoulders, ...) can indeed be explained by this effect. Moreover, it is clear that one can approximate such deformed peaks by a combination of just a few double Gaussians.

3. Deconvolution technique

The presence of the peak deformation effect is troublesome as it degrades the mass resolution. It makes it difficult to evaluate the presence of minor species, especially if deformed peaks overlap. It also prevents the application of the normal data treatment chain. This paper therefore introduces a technique that is capable of removing the peak deformation effect.

3.1. Problem formulation

The DFMS signal, after offset removal, mass calibration and detector gain correction, provides the number of ions that hit the MCP/LEDA during the exposure in the form of a spectrum $f(m)$ in a mass interval $[m_{\text{begin}}, m_{\text{end}}]$. Prior to processing such a spectrum, the remaining noise level $f_{\text{threshold}}$ is determined.

A number of ions with masses M_k , $k = 1, \dots, K$, are known to be found in the given mass interval. We distinguish between “basic” and “additional” ions ($K = K' + K''$). A “basic” ion has a mass peak that is (at least partially) unaffected by other overlapping mass peaks, so that there is no contribution from other ions in an interval $[m_{k,\text{start}}, m_{k,\text{stop}}]$ around M_k . For an “additional” ion no such interval is available. This is the case, for instance, for an ion whose mass peak forms a small contribution in the wings of a dominant species.

Let also the non-deformed peak shape $G(\mu; w_1, w_2, \alpha)$, the aforementioned double-Gaussian response of the MCP/LEDA detector, be given as a function of μ , the difference from the nominal ion mass. The normalisation $G(0; w_1, w_2, \alpha) = 1$ is used. This peak shape is considered to be the same whatever the mass, so that the mass peak due to ions with mass M_k in a non-deformed spectrum is given by $\epsilon_k G(m - M_k; w_1, w_2, \alpha)$, with ϵ_k the height of the peak. Given a Gaussian

$$g(\mu; w) = e^{-\frac{\mu^2}{w^2}}$$

with half-width w , the double-Gaussian response is written as

$$G(\mu; w_1, w_2, \alpha) = (1 - \alpha)g(\mu; w_1) + \alpha g(\mu; w_2), \quad (2)$$

where $0 \leq \alpha < 1$ and $w_2 > w_1$. The widths w_1 and w_2 , and the relative contribution α of the second Gaussian to the response, are to be determined in the course of the process.

In order to remove the peak deformation effect, the shape of a deformed peak must be determined. From the discussion in Section 2.2, it appears natural to express the deformed peak shape as a linear combination of a limited number of double-Gaussian response functions. Note, however, that as a consequence of the variable dispersion in the instrument the deformed peak shape may

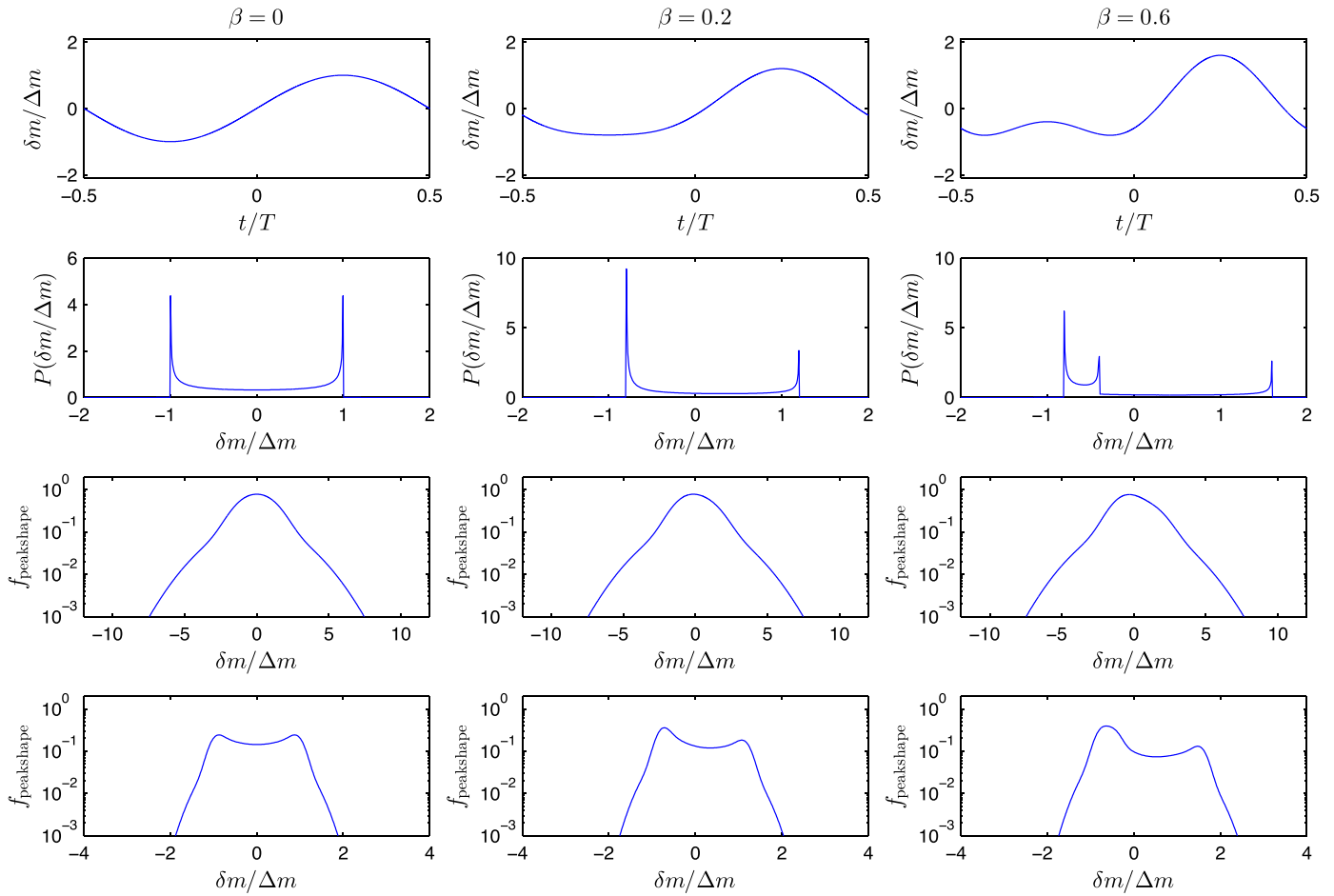


Fig. 4. Synthetic deformed peak shapes based on the fluctuation profile of Eq. (1). Left, middle, and right columns are for $\beta = 0, 0.2,$ and $0.6,$ respectively. From top to bottom: Waveform of the mass shift $\delta m/\Delta m$ as a function of time $t,$ the probability distribution $P(\delta m/\Delta m)$ of the mass shift, and the resulting mass peak shapes for $w_1/\Delta m = 1.28$ and $0.2,$ respectively, corresponding to DFMS peak shapes at low and high mass resolution.

change across the spectrum. The following form is adopted here for representing the peak shape around mass M_k :

$$P_k(m; \{\mu_j\}, \{\gamma_j\}, w_1, w_2, \alpha, \tau) = \sum_{j=1}^J \gamma_j G(m - m_{kj}(\mu_j, \tau); w_1, w_2, \alpha) \quad (3)$$

with the normalisation $\sum_j \gamma_j = 1.$ This expresses P_k as a linear combination of J double-Gaussians with coefficients $\gamma_j,$ all with the same $w_1, w_2,$ and α parameters. The double-Gaussians are located at masses $m_{kj} = M_k + s(M_k, \tau)\mu_j,$ where

$$s(M_k, \tau) = \frac{1 + \tau \left(\frac{M_k - m_{\text{mid}}}{m_{\text{range}}} \right)^2}{1 + \tau \left(\frac{M_1 - m_{\text{mid}}}{m_{\text{range}}} \right)^2},$$

with $m_{\text{mid}} = (m_{\text{begin}} + m_{\text{end}})/2$ and $m_{\text{range}} = (m_{\text{end}} - m_{\text{begin}})/2.$ The factor $s(M_k, \tau)$ is introduced to allow a variable spacing between the contributing double-Gaussians. It is assumed that there is a quadratically increasing dispersion away from the center of the spectrum, determined by parameter $\tau > 0.$ For the first basic mass M_1 the factor is $s(M_1, \tau) = 1$ and thus $m_{kj} = M_k + \mu_j,$ i.e., the μ_j express the relative positions of the contributing double-Gaussians to the mass associated with the deformed peak $P_1.$ For all other ions the peak is constructed by proportionally squeezing the double-Gaussians together or positioning them farther apart, resulting

in narrower or broader deformed peaks. Note, however, that the widths of the underlying double-Gaussians do not change. This is compatible with the idea that changes in the electrostatic analyser electric fields do not modify the beam-forming characteristics of the instrument but only lead to a displacement of the beam.

If the deformed peak shapes are known, the observed spectrum can be modelled as

$$f_{\text{model}}(m) = \sum_{k=1}^K \epsilon_k P_k(m; \{\mu_j\}, \{\gamma_j\}, w_1, w_2, \alpha, \tau) \quad (4)$$

with the ϵ_k giving the contribution of each of the K ions.

Correcting the peak deformation then amounts to solving an optimisation problem: Minimise the discrepancy between $f(m)$ and $f_{\text{model}}(m)$ by determining the optimal parameter values. First, there are the intensities $\epsilon_1, \dots, \epsilon_K$ of the deformed peaks at masses $\tilde{M}_1, \dots, \tilde{M}_K.$ Note that, because of possible minor errors in the mass calibration, these masses may differ slightly from the given ion masses M_1, \dots, M_K and must be considered unknown. Next, there are the unknown mass deviations μ_1, \dots, μ_j and the corresponding contributions $\gamma_1, \dots, \gamma_j,$ together with parameter $\tau,$ that define the deformed peak shape and how it changes across the spectrum. Note that we choose $\tilde{M}_1 = M_1;$ otherwise there would be an ambiguity in defining the $\mu_j.$ Finally, one has the parameters w_1, w_2 and α that describe the underlying double-Gaussian response. If one

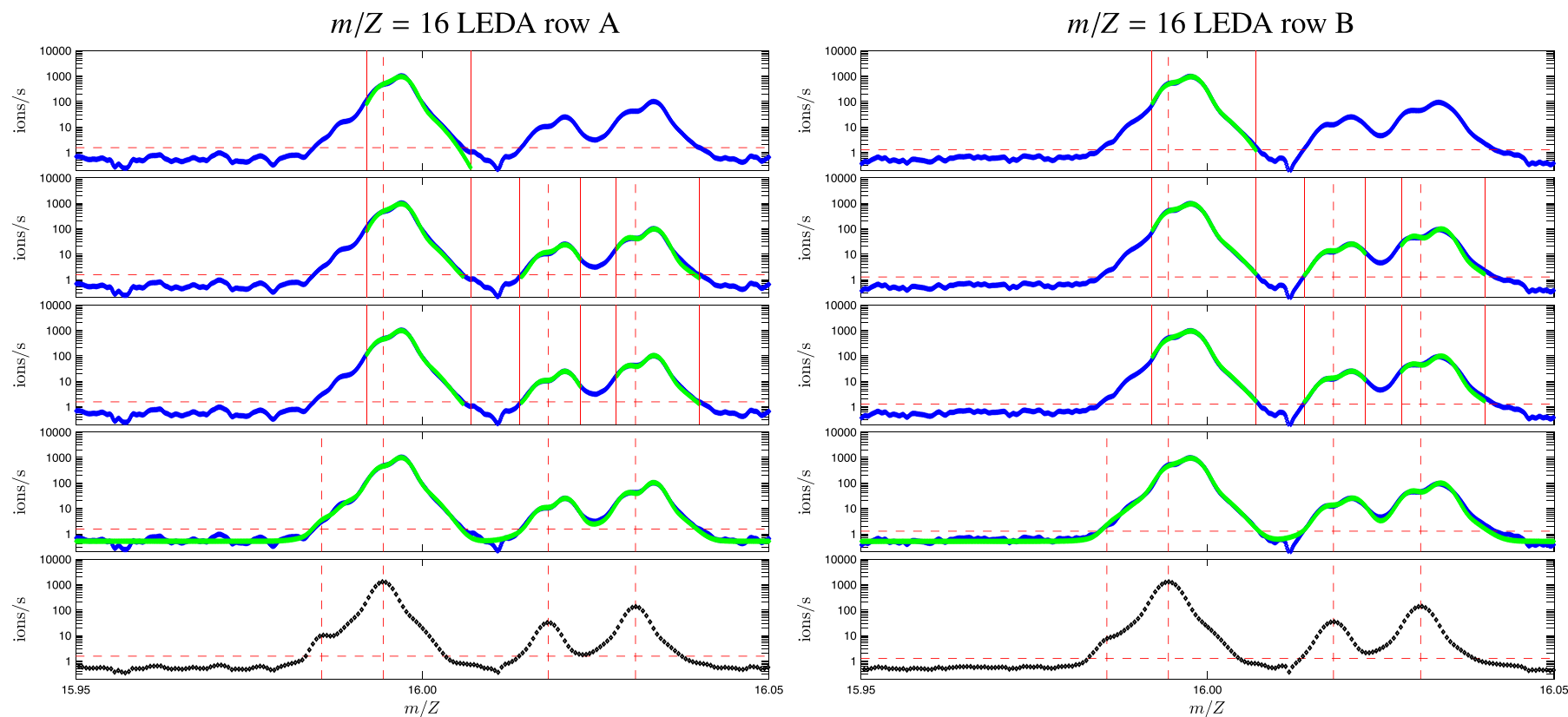


Fig. 5. Deformed peak shape correction for HR spectra at $m/Z=16$ on 2014-10-20 19:54:20. The panels show the calibrated spectrum in blue, with the model fit result after each step of the optimisation process in green, as explained in the [Appendix](#). The bottom panel gives the corrected spectrum. The peaks correspond to $^{32}\text{S}^{2+}$, $^{16}\text{O}^+$, $^{14}\text{NH}_2^+$, and $^{12}\text{CH}_4^+$, in order of increasing mass; their positions are indicated by the vertical dashed lines. The vertical solid lines demarcate the intervals where the fitting is performed for the basic ions. The horizontal dashed line gives the maximum noise level. (For interpretation of the references to color in this figure legend, the reader is referred to the web version of this article.)

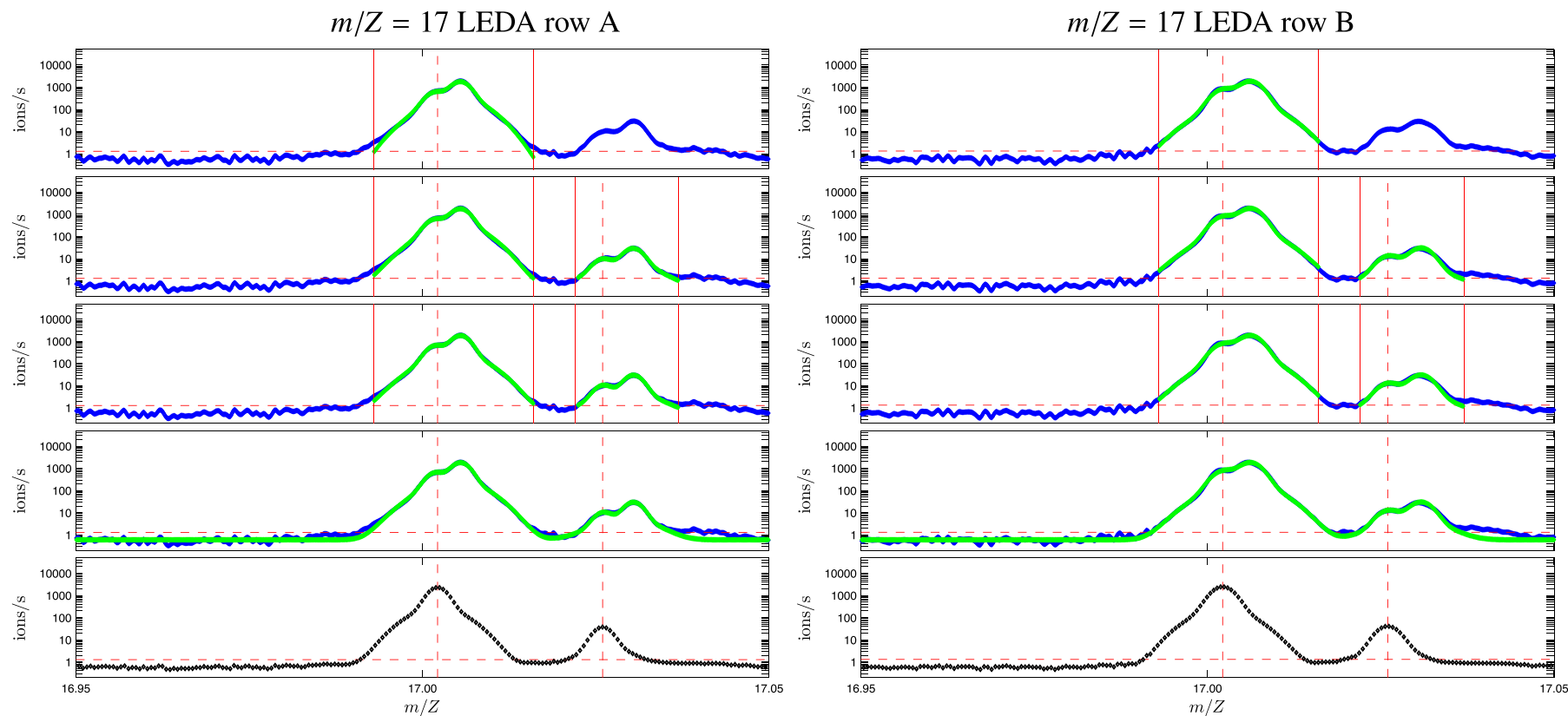


Fig. 6. Deformed peak shape correction for HR spectra at $m/Z=17$ on 2014-10-20 19:54:50. The panels show the calibrated spectrum in blue, with the model fit result after each step of the optimisation process in green, as explained in the [Appendix](#). The bottom panel gives the corrected spectrum. The peaks correspond to $^{16}\text{OH}^+$ and $^{14}\text{NH}_3^+$ in order of increasing mass; their positions are indicated by the vertical dashed lines. The vertical solid lines demarcate the intervals where the fitting is performed for the basic ions. The horizontal dashed line gives the maximum noise level. (For interpretation of the references to color in this figure legend, the reader is referred to the web version of this article.)

Table 1
Ions and masses in HR spectra at $m/Z = 16$.

Ion	Mass (amu/e)
$^{32}\text{S}^{2+}$	15.9855
$^{16}\text{O}^+$	15.9944
$^{14}\text{NH}_2^+$	16.0182
$^{12}\text{CH}_4^+$	16.0308

succeeds in solving this optimisation problem, one can construct the deconvolved spectrum

$$f_{\text{deconvolved}}(m) = \sum_{k=1}^K \epsilon_k G(m - m_k; w_1, w_2, \alpha). \quad (5)$$

Integrating the total detected signal under the deformed peak for an isolated ion k yields

$$\begin{aligned} \epsilon_k \int_{-\infty}^{+\infty} P_k(m) dm &= \epsilon_k \sum_{j=1}^J \gamma_j \int_{-\infty}^{+\infty} G(\mu) d\mu \\ &= \epsilon_k \int_{-\infty}^{+\infty} G(\mu) d\mu, \end{aligned}$$

that is, it is exactly identical to the signal under the deconvolved peak, as it should be. Note that changing the spacing of the contributing double-Gaussians as specified by τ has no influence on the total area under the deformed peak.

The optimisation problem sketched above is difficult to solve for three reasons. First, there typically are a large number of degrees of freedom. Second, the problem is nonlinear. Finally, there may be a number of suboptimal local minima. To make the problem tractable, it is necessary to break it down into a number of simpler steps. The Appendix describes in detail how this problem can be tackled.

3.2. Results

Fig. 5 shows the HR $m/Z = 16$ spectrum obtained by DFMS on 2014-10-20 19:54:20 for LEDA row A (left) and row B (right). We consider three basic ions, $^{16}\text{O}^+$, $^{12}\text{CH}_4^+$ and $^{14}\text{NH}_2^+$, in order of decreasing importance, and one additional ion, $^{32}\text{S}^{2+}$. The masses of these ions are given in Table 1. The calibrated spectrum after the usual (automated) approximate mass calibration, after removal of the LEDA offset and applying the gain and the pixel gain correction, and after enhancing the mass resolution $4\times$ (as explained in the Appendix), is given in the figure panels as a blue curve. The three major ions appear as double peaks with the peak to the low-mass side lower than the one at the high-mass side, or as peaks with a strong shoulder on the low-mass side: while the deformed peak for $^{16}\text{O}^+$ near the center looks like a single peak with a shoulder, the signature of $^{12}\text{CH}_4^+$ to the right is a double peak. The maximum noise level is given by the horizontal dashed line.

The result of the first optimisation step (first panel, green curve) is an initial approximation of the peak shape of the first basic species $^{16}\text{O}^+$ within the given interval demarcated by the solid vertical lines; only 2 double-Gaussians are used. The second panel gives the result of the second optimisation step in which this approximation is used to model the three basic species in the three demarcated intervals, by determining the parameter τ that describes how the peak shape changes across the spectrum. The third panel shows the output of an improved determination of the deformed peak shape, where more double-Gaussians are introduced (one more in this case). In the fourth panel this final deformed peak shape is used to also model the additional species. The corrected spectrum is given as the black curve in the bottom panel.

Table 2
Results for HR spectra at $m/Z = 16$ on 2014-10-20 19:54:20.

Subpeak	Row A		Row B	
	μ (amu/e)	γ	μ (amu/e)	γ
1	-0.0003	0.26234	0.0003	0.30929
2	0.0026	0.73614	0.0003	0.00093
3	0.0030	0.00152	0.0034	0.68978
Ion	\tilde{M} (amu/e)	ϵ (ions/s)	\tilde{M} (amu/e)	ϵ (ions/s)
$^{32}\text{S}^{2+}$	15.9863	9.0	15.9866	5.7
$^{16}\text{O}^+$	15.9944	1282.5	15.9944	1280.8
$^{14}\text{NH}_2^+$	16.0178	31.9	16.0171	34.4
$^{12}\text{CH}_4^+$	16.0302	135.9	16.0291	139.4
Parameter				
w_1	0.00161 amu/e		0.00190 amu/e	
w_2	0.00403 amu/e		0.00456 amu/e	
α	0.1071		0.0768	
τ	2.5490		3.6713	

Table 3
Ions and masses in HR spectra at $m/Z = 17$.

Ion	Mass (amu/e)
$^{16}\text{OH}^+$	17.0022
$^{14}\text{NH}_3^+$	17.0260

Table 2 lists the parameters that are retrieved for both LEDA rows. Typically, w_1 is larger for row B than for row A; this is believed to be due to slight differences in the focussing of the ion beam. Hence, row A is often preferred for data analysis since it yields a better mass resolution. At the same time, α is lower for row B. For both rows it seems that the deformed peaks are already well described by only 2 double Gaussians. For row A, 99.8% of the signal is captured by them, and for row B more than 99.9%. Overall, the results for row A and B are quite similar, leading to a quantitative assessment of the importance of the four ions relative to the maximum noise level $f_{\text{threshold}} \sim 1.5$ ions/s, about the same for both rows; note that the exposure lasted about 20 s. The end result reveals the contribution from $^{32}\text{S}^{2+}$. For row A an isolated $^{32}\text{S}^{2+}$ peak is seen, while for row B it forms a bump on the low-mass flank of the $^{16}\text{O}^+$ peak. This is mostly due to the larger w_1 and w_2 for row B; the difference in the $^{32}\text{S}^{2+}$ peak intensity is 30–40%. The values for the other peaks differ only by a few percent.

Analogously, Fig. 6 shows the HR $m/Z = 17$ spectrum obtained by DFMS on 2014-10-20 19:54:50 (blue curve), right after the one for $m/Z = 16$. We consider only 2 basic ions, namely $^{16}\text{OH}^+$ and

Table 4
Results for HR spectra at $m/Z = 17$ on 2014-10-20 19:54:50.

Subpeak	Row A		Row B	
	μ (amu/e)	γ	μ (amu/e)	γ
1	-0.0003	0.22952	0.0001	0.27600
2	0.0033	0.00068	0.0030	0.00988
3	0.0033	0.76980	0.0040	0.71411
Ion	\tilde{M} (amu/e)	ϵ (ions/s)	\tilde{M} (amu/e)	ϵ (ions/s)
$^{16}\text{OH}^+$	17.0022	2329.1	17.0022	2493.8
$^{14}\text{NH}_3^+$	17.0265	37.3	17.0260	40.7
Parameter				
w_1	0.00169 amu/e		0.00205 amu/e	
w_2	0.00453 amu/e		0.00488 amu/e	
α	0.1147		0.0919	
τ	3.0648		3.2265	

$^{14}\text{NH}_3^+$ in order of decreasing importance, and no additional ions; the masses are listed in Table 3. The optimisation procedure is simpler than for the $m/Z = 16$ case. The figure panels show the results of the successive optimisation steps. The model reconstruction of the deformed spectrum is shown in the fourth panel, while the bottom panel gives the deconvolved spectrum. Table 4 lists the parameters for both LEDA rows. The characteristic parameters w_1 , w_2 , α and τ are found to be largely similar to those in Table 2. The intensities ϵ obtained from rows A and B for both species differ again by only a few percent.

4. Discussion and conclusion

The Double Focusing Mass Spectrometer (DFMS) on the Rosetta spacecraft is plagued by minor deformation of the mass peaks in the high resolution spectra around $m/Z = 16$ and 17. The shape of the deformation slowly changes with time.

The most likely cause is an unstable electric potential in the electrostatic analyser. Modelling suggests that such electric potential variations would lead to an apparent shift of the peaks on the detector without modifying the actual beam-forming pattern, a typical double-Gaussian shape. One expects that the peaks observed after accumulating observations over a certain period of time can be approximated by a linear combination of a few double-Gaussians. In fact, two double-Gaussians often seem to capture 99% of the signal or more, indicating that the potential essentially alternates between two values. By examining how the deformed peak shape changes across the spectrum, it has been possible to confirm, at least to first order, that the beam pattern indeed is only shifted without changing its shape. The analysis presented here therefore appears to corroborate the conclusion that a deviation of the electric potential in the electrostatic analyser is indeed the cause of the problem.

At the same time the analysis suggests a technique for correcting the peak deformation. An algorithm has been developed and implemented, and the results for high resolution spectra at $m/Z = 16$ and 17 look promising. In this way, the processing of such spectra can be easily incorporated in the DFMS data analysis chain. This gives access to a few important ions, in particular $^{16}\text{O}^+$ and $^{16}\text{OH}^+$, that play a role in the water chemistry, which is essential for understanding the composition of cometary atmospheres. Also, some ions such as $^{32}\text{S}^{2+}$ become detectable, while they would otherwise have been missed. The typical differences in double-Gaussian peak shape between row A and B are consistently found in the results at both masses. The intensities obtained from both rows differ only by a few percent, except in the case of minor ions superimposed on the flanks of a major peak, where the results are more sensitive. There are a few caveats. First, the technique requires a sufficiently good mass calibration of the given spectrum. Also, it is hindered if the pixel gain correction is not sufficiently accurate, since that may affect the peak shape. In practice, these problems can appropriately be dealt with.

The unstable electric potential issue that has been studied here for DFMS mass spectra in neutral mode at $m/Z = 16$ and 17, will lead to deformations in the spectra at those masses in the ion mode as well. These may be, however, much harder to correct since the shape of the energy distribution of the particles is not a priori known (contrary to the double-Gaussian peak shape obtained in neutral mode).

Acknowledgements

The authors thank the following institutions and agencies, which supported this work: Work at BIRA-IASB was supported by the Belgian Science Policy Office via PRODEX/ROSINA PEA 90020 and an Additional Researchers Grant (Ministerial Decree of

2014-12-19), as well as by the Fonds de la Recherche Scientifique grant PDR T.1073.14 "Comparative study of atmospheric erosion". Work at UoB was funded by the State of Bern, the Swiss National Science Foundation, and by the European Space Agency PRODEX Program. Work at Southwest Research institute was supported by subcontract no. 1496541 from the Jet Propulsion Laboratory. This work has been carried out thanks to the support of the A*MIDEX project (n° ANR-11-IDEX-0001-02) funded by the "Investissements d'Avenir" French Government program, managed by the French National Research Agency (ANR). This work was supported by CNES grants at LATMOS and LPC2E. Work at the University of Michigan was funded by NASA under contract JPL-1266313. The results from ROSINA would not be possible without the work of the many engineers, technicians, and scientists involved in the mission, in the Rosetta spacecraft, and in the ROSINA instrument team over the past 20 years whose contributions are gratefully acknowledged. We thank herewith the work of the whole ESA/Rosetta team. Rosetta is an ESA mission with contributions from its member states and NASA. All ROSINA data are available on request until they are released to the PSA archive of ESA and to the PDS archive of NASA.

Appendix. Optimisation process

This appendix describes in detail how the optimisation problem discussed in this paper is actually solved.

Preprocessing step

The mass-calibrated and gain-corrected mass spectrum $f(m)$ is known at a set of discrete points (m_i, f_i) . However, it is clear that the underlying function f is continuously differentiable. To exploit this information to the fullest, the spectrum is interpolated to a $4\times$ better mass resolution using cubic spline interpolation. While this may seem to increase the amount of computational work, it leads to a smoother behaviour of the target functions in the optimisation problems outlined below and thus to better convergence properties. It is most appropriate to perform the interpolation on $\log f$.

Step 1

In a first step, the shape of the deformed peak around M_1 (usually the most pronounced peak in the spectrum) is determined approximately as a linear combination of J_0 double-Gaussians. This is achieved by minimising function

$$F_1^2 = \sum_i \beta_i \left[f_i - \sum_{j=1}^{J_0} \gamma_j' G(m_i - (M_1 + \mu_j); w_1, w_2, \alpha) \right]^2,$$

where the sum runs over all measurement points (m_i, f_i) that are within the unperturbed interval $m_i \in [m_{1,\text{start}}, m_{1,\text{stop}}]$ and that are above the noise level $f_i > f_{\text{threshold}}$, and where the parameters to fit are w_1 , w_2 , α , $\{\mu_j\}$ and $\{\gamma_j'\}$. The factor β_i is the weighting factor that is associated to each measurement. Choosing $\beta_i = 1$ would amount to fitting the measurements in absolute terms; given the high dynamic range of the measurements (up to 3–4 decades) one would fit the tip of the deformed peak, but not its flanks. Choosing $\beta_i = 1/f_i^2$ would fit the measurements in relative terms, which places equal weights on the tips and the flanks of the peaks. Here, the intermediate choice $\beta_i = 1/f_i$ is made, or, in order to ignore data below the noise threshold,

$$\beta_i = \frac{f_i}{f_i^2 + f_{\text{threshold}}^2}.$$

The problem is simplified by fixing $w_2 = 2.5w_1$, mainly to avoid situations with multiple local minima. We first solve the problem with a single double-Gaussian, $J_0 = 1$, thus approximating the deformed peak with a non-deformed one; this is a problem in μ_1 , γ'_1 , w_1 and α . We then progressively add double-Gaussians and try to improve on the overall fit. In each step, the initial values for the minimisation are found by re-using $\alpha|_{J_0} = \alpha|_{J_0-1}$, by taking $w_1|_{J_0} = w_1|_{J_0-1}(J_0 - 1)/J_0$, and by adopting $\mu_j|_{J_0} = \mu_j|_{J_0-1}$, $j = 1, \dots, J_0 - 1$ and locating μ_{J_0} where the residual of the approximation remains largest.

Since the system $\partial F_1^2 / \partial \gamma_j = 0$, $j = 1, \dots, J_0$ is linear, one finds the optimal values of the γ_j for any given set of $\{\mu_j\}$, w_1 , and α from solving the overdetermined linear system

$$\sum_{j=1}^{J_0} A_{ij} \gamma'_j = b_i$$

with

$$A_{ij} = \beta_i G(m_i - (M_1 + \mu_j); w_1, w_2, \alpha),$$

$$b_i = \beta_i f_i.$$

This system is solved in a least-squares sense by making use of the generalised inverse of the rectangular coefficient matrix. This system is overdetermined only if one keeps J_0 low; if not, one is “overfitting” the problem. One should definitely never use more double-Gaussians than the number of pixels over which the deformed peak is smeared out, and that number is quite limited (maximum ~ 10). Another reason to limit J_0 is to keep the computational cost down. It turns out that using only $J_0 = 2$ is already a very good choice. In view of the results found in Fig. 4 (left column), this suggests that the oscillating electric field is actually better represented by a square wave than a sinusoidal one.

After the fitting process ends, the coefficients are normalised,

$$\gamma_j = \frac{\gamma'_j}{\sum_j \gamma'_j},$$

so that they can be used in the expression for the peak shape of Eq. (3).

Step 2

In the second step, we determine the parameter τ . This is done by applying the peak shape found in the first step to all basic ions; if only one basic ion mass is given, parameter value $\tau = 0$ is adopted. The value of τ can only be established while simultaneously determining \tilde{M}_k and ϵ_k for all basic ions. The target function to be minimised is

$$F_2^2 = \sum_i \beta_i \left[f_i - \sum_{k=1}^{K'} \epsilon_k P_k(m_i; \{\mu_j\}, \{\gamma_j\}, w_1, w_2, \alpha, \tau) \right]^2,$$

where $\{\mu_j\}$, $\{\gamma_j\}$, w_1 , w_2 , and α are the values obtained from the previous step. The sum runs over all points $m_i \in \bigcup_{k=1, \dots, K'} [m_{k, \text{start}}, m_{k, \text{stop}}]$ for which the measured signal is above the noise level. The same weighting factor β_i is used as before.

For given τ and \tilde{M}_k , one can find the ϵ_k from the linear system $\partial F_2^2 / \partial \epsilon_k = 0$, $k = 1, \dots, K'$. The overdetermined system is given by

$$A_{ij} = \beta_i P_k(m_i; \{\mu_j\}, \{\gamma_j\}, w_1, w_2, \alpha, \tau),$$

$$b_i = \beta_i f_i.$$

At the end of this step, an initial representation of the deformed peak and how it changes across the spectrum is established.

Step 3

In the third step the deformed peak shape is improved by adding double-Gaussians to the representation. At the same time, the values of w_1 , w_2 (which is now no longer tied to that of w_1), α and τ are improved. The set of $\{\mu_j\}$ and $\{\gamma_j\}$ is progressively extended and optimised, and also $\{\tilde{M}_k\}$ and $\{\epsilon_k\}$ are fine-tuned. This is done while repeatedly fitting

$$F_3^2 = F_2^2 + \left(\sum_j \gamma_j - 1 \right)^2 + c \left(\frac{w_2/w_1}{2.50} - 1 \right)^2$$

over the same set of points as in step 2. The first additional term in the target function serves to ensure the normalisation of the γ_j (if not, the solution is not uniquely defined and the optimisation problem is bound not to converge). The second additional term, with $0 \leq c \ll 1$, guides the value of w_2 relative to w_1 in order to regularise the problem, where a default value $w_2/w_1 = 2.50$ is used. In the expression for the deformed peak shape the number of double-Gaussians is progressively increased to a final value $J \leq J_0$; a value of only $J = 3$ is used routinely. Note that this optimisation process again can benefit from establishing the values of ϵ_k from an overdetermined linear system for given values of all other parameters.

This third step is computationally demanding since most of the problem parameters are to be optimised simultaneously. The goal of step 1 and 2 is exactly to provide a good initial solution for the big optimisation problem of step 3. First, given a good initial solution, the amount of work needed to find the optimum remains limited. Second, since the problem is so nonlinear, a good initial solution in the neighbourhood of the global optimum is a prerequisite to find that global optimum without getting stuck in some local minimum.

Step 4

The result from the previous step is an accurate representation of the deformed peaks and how they change across the spectrum. This can now be used to fit the full deformed spectrum, including also the additional ions. The target function is

$$F_4^2 = \sum_i \beta_i \left[f_i - \sum_{k=1}^K \epsilon_k P_k(m_i; \{\mu_j\}, \{\gamma_j\}, w_1, w_2, \alpha, \tau) \right]^2$$

where the sum now runs over all K ions and over all points (m_i, f_i) in the spectrum. The unknowns are the \tilde{M}_k (except $\tilde{M}_1 = M_1$) and ϵ_k ; all other quantities are given. Again, for any set of values $\{\tilde{M}_k\}$ one can obtain the ϵ_k from the overdetermined linear system already used in step 2.

Postprocessing step

As already outlined, once all the parameters have been computed, it is possible to determine the deconvolved spectrum $f_{\text{deconvolved}}$ according to Eq. (5), interpolated back to the original mass scale. The corrected spectrum is defined as

$$f_{\text{corrected}} = \xi(f_{\text{deconvolved}} + f_{\text{noise}}) + (1 - \xi)f,$$

that is, a linear combination of the deconvolved spectrum (adding the average noise level) and the observed spectrum, where ξ varies between 0 and 1 depending on how much the observations are above the noise level; here, the choice

$$\xi = \frac{1}{2} + 4 \left(\frac{f^2}{f^2 + f_{\text{noise}}^2} - \frac{1}{2} \right)^3$$

was made.

Optimisation technique

The optimisation technique used is a combination of a stochastic search method that probes the environment of a current set of parameter values, and the Broyden–Fletcher–Goldfarb–Shanno algorithm [13,14] that starts as a steepest descent technique and progressively evolves to the Newton algorithm as it collects information about the Hessian of the target function near the optimum. To improve the numerical behaviour, the optimisation parameters are judiciously rescaled.

The optimisation strategy also allows to impose bounds on some of the parameters. If a parameter p should not exceed a limit value p^* , the target function $F(p)$ is modified into

$$F'(p) = F(\min\{p, p^*\})[1 + (\max\{p - p^*, 0\})^2],$$

so that $F'(p) \equiv F(p)$ inside the allowed domain, and $F'(p) > F(p^*)$ outside. In practice, such bounds have been introduced so that

$$\begin{aligned} 0.50w_0 &\leq w_1 \leq 2w_0, \\ 1.25w_0 &\leq w_2 \leq 5w_0, \\ 0.075 &\leq \alpha \leq 0.30, \\ 0 &\leq \tau \end{aligned}$$

Furthermore, precautions have been taken to keep all \tilde{M}_k close to the corresponding M_k , and to keep all $\gamma_j \geq 0$ and $\epsilon_k \geq 0$.

Appendix A. Supplementary data

Supplementary data associated with this article can be found, in the online version, at <http://dx.doi.org/10.1016/j.ijms.2015.10.010>

References

- [1] H. Balsiger, K. Altwegg, P. Bochsler, P. Eberhardt, J. Fischer, S. Graf, A. Jäckel, E. Kopp, U. Langer, M. Mildner, J. Müller, T. Riesen, M. Rubin, S. Scherer, P. Wurz, S. Wüthrich, E. Arijs, S. Delanoye, J. De Keyser, E. Neefs, D. Nevejans, H. Rème, C. Aoustin, C. Mazelle, J.-L. Médale, J.A. Sauvaud, J.-J. Berthelier, J.-L. Bertaux, L. Duvet, J.-M. Illiano, S.A. Fuselier, A.G. Ghielmetti, T. Magoncelli, E.G. Shelley, A. Korth, K. Heerlein, H. Lauche, S. Livi, A. Loose, U. Mall, B. Wilken, F. Gliem, B. Fiethe, T.I. Gombosi, B. Block, G.R. Carignan, L.A. Fisk, J.H. Waite, D.T. Young, H. Wollnik, Rosina – Rosetta Orbiter Spectrometer for Ion and Neutral Analysis, *Space Sci. Rev.* 128 (1–4) (2007) 745–801, <http://dx.doi.org/10.1007/s11214-006-8335-3>.
- [2] S. Wüthrich, Characterization of the ROSINA DFMS Instrument by Numerical Modeling (Ph.D. thesis), Physikalisches Institut, Universität Bern, Switzerland, 2007.
- [3] J.-J. Berthelier, J.-M. Illiano, D. Nevejans, E. Neefs, E. Arijs, N. Schoon, High resolution focal plane detector for a space-borne magnetic mass spectrometer, *Int. J. Mass Spectrom.* 215 (1–3) (2002) 89–100, [http://dx.doi.org/10.1016/S1387-3806\(02\)00527-4](http://dx.doi.org/10.1016/S1387-3806(02)00527-4).
- [4] D. Nevejans, E. Neefs, S. Kavadias, P. Merken, C. Van Hoof, The LEDA512 integrated circuit anode array for the analog recording of mass spectra, *Int. J. Mass Spectrom.* 215 (1) (2002) 77–87, [http://dx.doi.org/10.1016/S1387-3806\(01\)00549-8](http://dx.doi.org/10.1016/S1387-3806(01)00549-8).
- [5] M. Hässig, K. Altwegg, H. Balsiger, J.-J. Berthelier, U. Calmonte, M. Combi, J. De Keyser, B. Fiethe, S.A. Fuselier, M. Rubin, ROSINA/DFMS capabilities to measure isotopic ratios in water at comet 67P/Churyumov-Gerasimenko, *Planet. Space Sci.* 84 (2013) 148–152, <http://dx.doi.org/10.1016/j.pss.2013.05.014>.
- [6] M. Hässig, K. Altwegg, J.-J. Berthelier, U. Calmonte, J. De Keyser, B. Fiethe, S.A. Fuselier, T.I. Gombosi, L. Le Roy, T. Owen, M. Rubin, The capabilities of ROSINA/DFMS to measure argon isotopes at comet 67P/Churyumov-Gerasimenko, *Planet. Space Sci.* 105 (2015) 175–178, <http://dx.doi.org/10.1016/j.pss.2014.11.015>.
- [7] K. Altwegg, H. Balsiger, U. Calmonte, M. Hässig, L. Hofer, A. Jäckel, B. Schläppi, P. Wurz, J.-J. Berthelier, J. De Keyser, B. Fiethe, S.A. Fuselier, U. Mall, M. Rubin, H. Rème, In situ mass spectrometry during the Lutetia flyby, *Planet. Space Sci.* 66 (1) (2012) 173–178.
- [8] K. Altwegg, H. Balsiger, A. Bar-Nun, J.-J. Berthelier, A. Bieler, P. Bochsler, C. Briois, U. Calmonte, M. Combi, J. De Keyser, P. Eberhardt, B. Fiethe, S.A. Fuselier, S. Gasc, T.I. Gombosi, K.C. Hansen, M. Hässig, A. Jäckel, E. Kopp, A. Korth, L. Le Roy, U. Mall, B. Marty, O. Mousis, E. Neefs, T. Owen, H. Rème, M. Rubin, T. Sémon, C.-Y. Tzou, H. Waite, P. Wurz, 67P/Churyumov-Gerasimenko a Jupiter family comet with a high D/H ratio, *Science* 347 (6220) (2014) 1261952, <http://dx.doi.org/10.1126/science.1261952>.
- [9] M. Hässig, K. Altwegg, H. Balsiger, A. Bar-Nun, J.-J. Berthelier, A. Bieler, P. Bochsler, C. Briois, U. Calmonte, M. Combi, J. De Keyser, P. Eberhardt, B. Fiethe, S.A. Fuselier, M. Galand, S. Gasc, T.I. Gombosi, K.C. Hansen, A. Jäckel, H.U. Keller, E. Kopp, A. Korth, E. Kührt, L. LeRoy, U. Mall, B. Marty, O. Mousis, E. Neefs, T. Owen, H. Rème, M. Rubin, T. Sémon, C. Tornov, C.-Y. Tzou, H. Waite, P. Wurz, Time variability and heterogeneity in the coma of 67P/Churyumov-Gerasimenko, *Science* 347 (6220) (2015) aaa0276, <http://dx.doi.org/10.1126/science.aaa0276>.
- [10] M. Rubin, K. Altwegg, H. Balsiger, A. Bar-Nun, J.-J. Berthelier, A. Bieler, P. Bochsler, C. Briois, U. Calmonte, M. Combi, J. De Keyser, F. Dhooche, P. Eberhardt, B. Fiethe, S.A. Fuselier, S. Gasc, T.I. Gombosi, K.C. Hansen, M. Hässig, A. Jäckel, E. Kopp, A. Korth, L. Le Roy, U. Mall, B. Marty, O. Mousis, T. Owen, H. Rème, T. Sémon, C.-Y. Tzou, H. Waite, P. Wurz, Molecular nitrogen in comet 67P/Churyumov-Gerasimenko indicates a low formation temperature, *Science* 348 (6231) (2015) 232–235, <http://dx.doi.org/10.1126/science.aaa6100>.
- [11] E.G. Johnson, A.O. Nier, Angular aberrations in sector shaped electromagnetic lenses for focusing beams of charged particles, *Phys. Rev.* 91 (1953) 10–17.
- [12] M. Hässig, Sensitivity and Fragmentation Calibration of the ROSINA Double Focusing Mass Spectrometer (Ph.D. thesis), Universität Bern, 2013.
- [13] C.G. Broyden, The convergence of a class of double-rank minimization algorithms, *J. Inst. Math. Appl.* 6 (1) (1970) 76–90, <http://dx.doi.org/10.1093/imamat/6.1.76>.
- [14] R. Fletcher, A new approach to variable metric algorithms, *Comput. J.* 13 (3) (1970) 317–322, <http://dx.doi.org/10.1093/comjnl/13.3.317>.